A Harmonic Decomposition Reconstruction Algorithm for Spatially Varying Focal Length Collimators

Jiangsheng You,* *Member, IEEE*, Zhengrong Liang, *Member, IEEE*, and Shanglian Bao

***Abstract*—Spatially varying focal length fan-beam collimators can be used in single photon emission computed tomography to improve detection efficiency and to reduce reconstruction artifacts resulting from the truncation of projection data. It has been proven that there exists no convolution backprojection algorithm for this type of collimator, so a complicated interpolation between two nonparallel projection rays is necessary for existing algorithms. The interpolation may generate blurring and artifacts in the reconstructed images. Based on a harmonic decomposition technique and the translation property of Fourier series, a semifrequency resampling technique is proposed to avoid the above mentioned interpolations. By this technique, the harmonic decomposition of projection data for spatially varying focal length fan-beam collimators has the same form as that for parallel-beam collimators in the semifrequency domain (Fourier transform with respect to angular variables only). An alternative version of the inverse Cormack transform is then proposed to reconstruct the images. The derived reconstruction algorithm was implemented in a Pentium II/266 PC computer. Numerical simulations demonstrated its efficiency (3 s for 128×128 reconstruction arrays) and its robust performance (compared to the existing algorithms).**

***Index Terms*— Harmonic decomposition, inverse Cormack transform, spatially varying focal length fan-beam geometry.**

I. Introduction

In single photon emission computed tomography (SPECT), a fan-beam collimator with spatially varying focal lengths can be used with a gamma camera to improve detection efficiency and to reduce reconstruction artifacts due to the truncation of projection data. The focal lengths increase from a minimum at the center to a maximum at the edge of the object (see Fig. 1). Thus, those projection rays with short focal lengths improve detection efficiency in the central region of interest (ROI) and others with long focal lengths avoid truncation artifacts near the edge of the object. The development of an accurate and efficient reconstruction algorithm for such a data acquisition geometry is a topic of research interest.

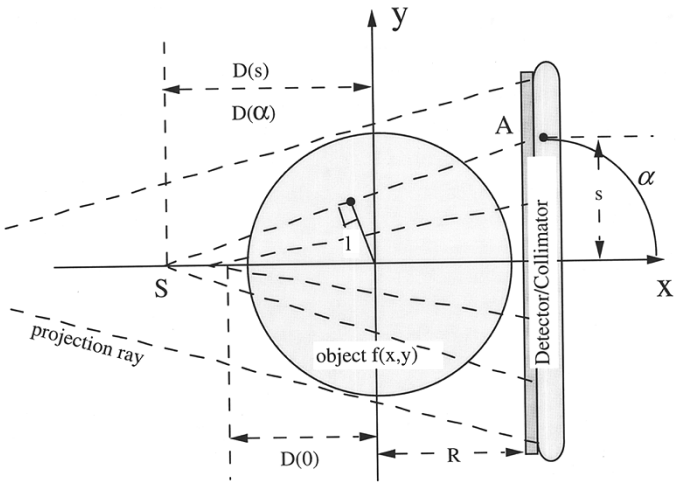

Fig. 1. Illustration of the spatially varying focal length fan-beam geometry. The focal length function $D(\cdot)$ can be expressed by either the angular coordinate α or the distance coordinate s. $D(\alpha)$ varies slowly near $\alpha = 0$ and changes fast when $|\alpha|$ increases.

Convolution backprojection algorithms were developed for parallel-hole collimators [1] and later extended to various fan-beam geometries [2]–[4], and have demonstrated their accuracy and efficiency. It has been proven that there exists no convolution backprojection algorithm for spatially varying focal length fan-beam geometry [5]. Zeng *et al*. proposed a summed filtered-backprojection algorithm to reconstruct the image approximately [6]. Cao and Tsui performed the double integrals for the reconstruction problem for these types of geometries and this required intensive computation [7]. Recently, Zeng and Gullberg implemented a backprojection filtering algorithm to reconstruct the image more accurately [8]. Although the above efforts succeed in some degrees, further investigation for improvement of these existing algorithms or development of accurate and efficient algorithms are needed. Since the sampled projection data are not uniformly distributed in the polar coordinates in the projection space, these existing algorithms require an interpolation between two nonparallel projection rays. The interpolation may generate blurring and artifacts in the reconstructed images. To minimize the interpolation errors, we had proposed a fast resorting technique to rebin the projec-

Manuscript received December 12, 1996; revised September 22, 1998. This work was supported in part by the National Natural Science Fondation (NNSF) of China under Grants 39570223 and 19675005, in part by the National Institutes of Health (NIH) under Grants HL51466 and NS 35853, and in part by the American Heart Association under EI Awards. The Associate Editor responsible for coordinating the review of this paper and recommending its publication was G. T. Gullberg. *Asterisk indicates corresponding author.*

*J. You was with the Institute of Heavy Ion Physics, Peking University, Beijing 100871, P.R. China. He is now with the Department of Radiology, SUNY, Stony Brook, NY 11794 USA.

Z. Liang is with the Departments of Radiology and Computer Science, and the Biomedical Engineering Program, SUNY, Stony Brook, NY 11794 USA.

S. Bao is with the Institute of Heavy Ion Physics, Peking University, Beijing 100871, P.R. China.

Publisher Item Identifier S 0278-0062(98)09418-X.

tion data under the constraint that both the angular increment between successive projections and the angular increment between rays in each projection were the same constant [5]. However, in practice, the sampled data are not always the case assumed in [5], therefore, further research is necessary toward accurate and efficient reconstruction similar to the convolution backprojection procedure. In this paper, we extend our previous work [5] to achieve the goal of developing an accurate and efficient reconstruction similar to the convolution backprojection algorithm. Based on the harmonic decomposition technique and the translation property of Fourier series, a semifrequency resampling technique is developed to reduce the interpolation artifacts and to improve the computational efficiency. An alternative version of the inverse Cormack transform is then proposed to reconstruct the images. Both equiangular sampling and equally spaced sampling for the projection data are investigated. The developed algorithm is as accurate and efficient as the convolution backprojection algorithm.

This paper is organized as follows. In Section II, detailed illustrations for the collimator geometry and the sampled grids are presented. In Section III, a brief review of the inverse Cormack transform is given and a simple translation property of Fourier series is introduced. Then, by the radon inversion formula, we obtain an alternative version of the inverse Cormack transform for image reconstruction. In Section IV, several computer simulations are conducted to show the performance of the developed algorithm.

II. Collimator Geometry

The detector geometry discussed in this paper is shown in Fig. 1. Assume that the flat detector is parallel to the y-axis with a distance R away from the origin. The detected value at a point A on the detector is the integral of radionuclide distribution $f(x,y)$ along line SA, where S is located on the x-axis. Let α denote the angle between the line SA and the x-axis. The focal point S has a varying distance $D(\alpha)$ from the origin. When the focal length increases from a minimum for rays passing through the center to a maximum for rays passing through the edge of the object, $D(\alpha)$ should increase with $|\alpha|$. Every projection ray in Fig. 1 can be determined uniquely by the departure angle α.

After the detector is rotated around the origin from the position of Fig. 1 by an angle Φ (see Fig. 2), every point on the detector can be uniquely determined by either angular coordinate (Φ,α) or distance coordinate (Φ,s). Comparing with the parallel-beam coordinate (l,θ), we have the following relations for the angular coordinate

$$l = D(\alpha)\sin\alpha \quad \text{and} \quad \theta = \Phi + \frac{\pi}{2} + \alpha. \tag{1}$$

The Jacobian from $d\alpha\, d\Phi$ to $dl\, d\theta$ is

$$J(\alpha) = D'(\alpha)\sin\alpha + D(\alpha)\cos\alpha \tag{2}$$

where $D'(\alpha)$ is the derivative of $D(\alpha)$ with respect to α.

As presented in [6]–[8], the projection data are not always sampled with a uniform α increment, although there are many advantages of using the angular expressions [5]. In fact, the angular expression is equivalent to the distance coordinate

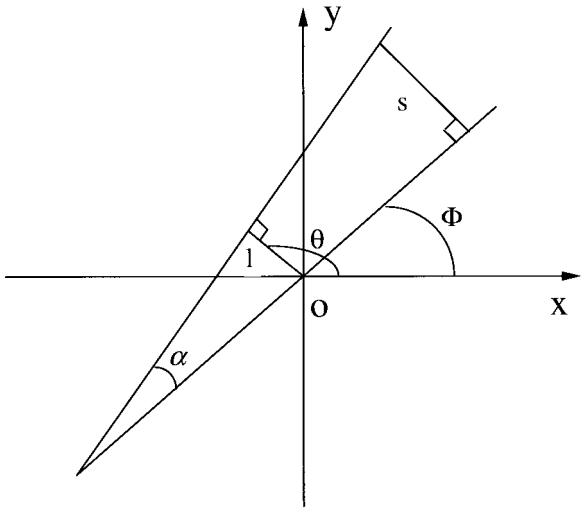

Fig. 2. Graphic representation of the angular coordinate (Φ,α), distance coordinate (Φ,s) and the parallel-beam coordinate (l,θ).

representation under a one-to-one mapping

$$\alpha = \tan^{-1}\left[\frac{s}{D(s)+R}\right]. \tag{3}$$

In this paper, we will present some comparison studies using both uniform α increment and uniform s increment in projection data generation. Both coordinate expressions will be used in derivation and implementation of the presented algorithm. For details of the distance coordinate (Φ,s), see the illustrations in Figs. 1 and 2, and the following arguments.

Let $R_0 = \min\{D(0), R\}$ and $B(R_0)$ denote a disk of radius R_0 centered at the origin. Obviously, the Jacobian $J(\alpha) \neq 0$ inside this disk. We assume that the support of the radionuclide distribution $f(x,y)$ is contained in $B(R_0)$. Let $P(\Phi,s)$ be the detected projection datum at point (Φ,s) on the detector, and $p(l,\theta)$ denote its parallel-beam expression, then $P(\Phi,s) = p(l,\theta)$ when

$$l = \frac{sD(s)}{\sqrt{\left(D(s)+R\right)^2 + s^2}} \tag{4}$$

and

$$\theta = \Phi + \frac{\pi}{2} + \tan^{-1}\left(\frac{s}{D(s)+R}\right). \tag{5}$$

Notice that $D(s)$ and $D(\alpha)$ are different expressions of the same distance. But, the expressions of (1) are simpler than those of (4) and (5).

Suppose that the subtending angle of $P(\Phi,\alpha)$ is $2\alpha_0$, i.e., $\alpha \in [-\alpha_0, \alpha_0]$, where $\alpha_0 < \frac{\pi}{2}$. To acquire complete projections for spatially varying focal length fan-beam geometry, Φ should rotate from $-\frac{\pi}{2}-\alpha_0$ to $\frac{\pi}{2}+\alpha_0$. Actually, $P(\Phi,\alpha)$ with $\Phi \in [0, 2\pi]$ and $\alpha \in [0, \alpha_0]$ form a complete set.

In the discrete case of data acquisition, Φ is evenly sampled in $[0, 2\pi]$ at M points and s is evenly sampled on $[-s_0, s_0]$ at N points when using the distance coordinate (Φ,s), where s_0 satisfies $\alpha_0 = \tan^{-1}[\frac{s_0}{D(s_0)+R}]$. In other words, $P(\Phi,s)$ are detected on (Φ_j, s_k), where $\Phi_j = j\delta_1$, $j = 0, 1, \cdots, M-1$,

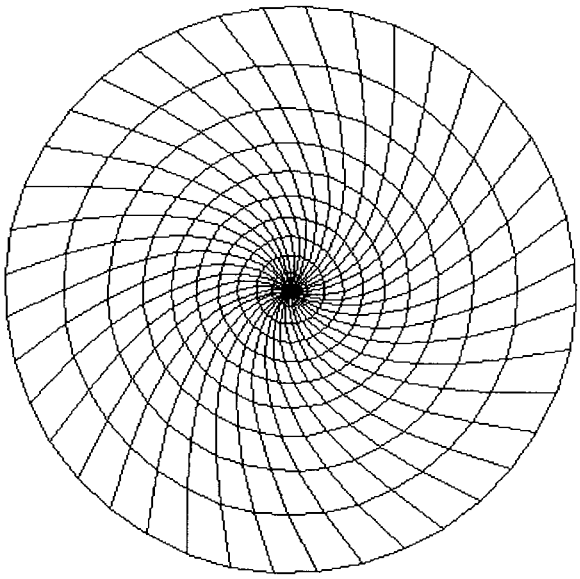

Fig. 3. The intersection points of the curves with the circles denote the sampled array (l_k, θ_j), derived from sampled array (Φ_j, s_k), in the projection space for spatially varying focal length fan-beam geometry with a function $D(s) = 2.0/\cos\alpha(s)$, where $\alpha(s)$ is given by (3). The radius of each circle is determined by the distance variable l_k of (4), given s_k. The position on each circle is specified by the angular variable θ of (5), which is determined by Φ and s. Given s_k, each sampled point θ_j on the circle l_k is related to the sample Φ_j by (5). Therefore, samples (l_k, θ_j) and (Φ_j, s_k) are related to each other. This relationship can be applied to samples (l_k, θ_j) and (Φ_j, α_k) for angular coordinate. Given θ_j, the line connecting all points (l_k, θ_j) is a curve, in contrast to the straight line in Fig. 4. The radius difference $(l_{k+1} - l_k)$ increases when l_k increases in Fig. 3, in contrast to the constant difference of $l_{k+1} - l_k$ in Fig. 4.

and $s_k = k\delta_2 - s_0$, $k = 0, 1, \cdots, N$ with $\delta_1 = \frac{2\pi}{M}$, $\delta_2 = \frac{2s_0}{N}$. For a specific focal-length function $D(s) = 2/\cos\alpha(s)$, where $\alpha(s)$ is related to s by (3), the sampled points (Φ_j, s_k) can be mapped to (l_k, θ_j), as shown in Fig. 3, where both Φ and s are uniformly sampled with increments δ_1 and δ_2, respectively. Notice that for every fixed s_k, $\{\theta_j\}$ or $\{\Phi_j\}$ are evenly located on the corresponding circle in Fig. 3. Obviously, the sampled array of Fig. 3 is less uniform than that of Fig. 4 for a parallel-beam geometry. Conventionally, the distance coordinate (Φ, s) is used to develop image reconstruction algorithms [6]–[8]. However, by our previous work [5], the angular expression may have several benefits in developing reconstruction algorithms for spatially varying focal length fan-beam geometries. So, both coordinate expressions were used in the computer simulations, as presented later.

III. Theory

In this section, the basic theory for the proposed reconstruction algorithm and its implementation are presented.

A. Review of the Inverse Cormack Transform

Let $f(r, \varphi)$ denote the polar coordinate expression of the radionuclide distribution $f(x, y)$. Since it is a periodic function for the angular variable φ, $f(r, \varphi)$ can be expanded as a Fourier series with respect to φ

$$f(r, \varphi) = \sum_{n=-\infty}^{\infty} f_n(r) e^{in\varphi}. \tag{6}$$

The radon transform $p(l, \theta)$ of $f(r, \varphi)$ is also a 2π periodic function with respect to the angular variable θ, its Fourier expansion is

$$p(l, \theta) = \sum_{n=-\infty}^{\infty} p_n(l) e^{in\theta}. \tag{7}$$

The relation between $f_n(r)$ and $p_n(l)$ is given in [9] and [10] as

$$p_n(l) = 2\int_l^{\infty} \frac{T_{|n|}\left(\frac{l}{r}\right) f_n(r) r}{\sqrt{r^2 - l^2}}\, dr \tag{8}$$

$$f_n(r) = -\frac{1}{\pi}\int_r^{\infty} \frac{T_{|n|}\left(\frac{l}{r}\right) p_n'(l) r}{\sqrt{l^2 - r^2}}\, dl \tag{9}$$

where $T_{|n|}(\cdot)$ is the nth order Chebyshev polynomial of the first kind and $p_n'(l)$ is the derivative of $p_n(l)$ with respect to l. Equations (8) and (9) are usually called the Cormack transform and inverse Cormack transform, respectively. By (9), we can reconstruct the image $f(r, \varphi)$ from its radon transform $p(l, \theta)$. However, as pointed out in [10] and [11], (9) is unstable in a numerical sense. To overcome this problem, a modified form of (9) is then given in [10] and [11]

$$\begin{aligned} f_n(r) = &-\frac{1}{r\pi} \\ &\times \left\{ \int_r^{\infty} \left(\frac{l^2}{r^2} - 1\right)^{-\frac{1}{2}} \left[\frac{l}{r} + \sqrt{\frac{l^2}{r^2} - 1}\right]^{-|n|} p_n'(l)\, dl \right. \\ &\left. - \int_0^r U_{|n|-1}\left(\frac{l}{r}\right) p_n'(l)\, dl \right\} \end{aligned} \tag{10}$$

where

$$U_n(x) = \frac{\sinh((n+1)\operatorname{arccosh}(x))}{\sinh(\operatorname{arccosh}(x))}$$

is the nth order Chebyshev polynomial of the second kind and $U_{-1} = 0$. (For details, see [10] and [11].) Rewrite (10) as

$$\begin{aligned} f_n(r) = &-\frac{1}{r\pi} \\ &\times \left\{ \int_r^{\infty} \left(\frac{r}{l}\right)^{|n|+1} \left(1 + \sqrt{1 - \frac{r^2}{l^2}}\right)^{-|n|} p_n'(l) \right. \\ &\left. \times d\sqrt{l^2 - r^2} - \int_0^r \frac{\sin\left(|n| \arccos\left(\frac{l}{r}\right)\right)}{\sin\left(\arccos\left(\frac{l}{r}\right)\right)} p_n'(l)\, dl \right\}. \end{aligned} \tag{11}$$

By an exponential transform, (11) can be expressed as a convolution [11]. Therefore, a fast Fourier transform (FFT) can be used to evaluate (11). When $r = 0$, the right side of (11) contains a singular term $\frac{1}{\sqrt{l^2 - r^2}}$ at $l = 0$. But from the identity

$$2\pi p_0(l) = \int_0^{2\pi} p(l, \theta)\, d\theta = \frac{1}{2}\int_0^{2\pi} (p(-l, \theta) + p(l, \theta))\, d\theta \tag{12}$$

and because $p_0(l)$ is an even function, if $f(x, y)$ is continuously differentiable, $p_0'(0) = 0$, and the singularity is avoided. This fact is very useful in numerical implementation. It is noted that the computation of the derivative $p_n'(l)$ and

the exponential transform in [11] are required. Usually, the computation of $p_n'(l)$ is implemented through a difference quotient which may generate extra errors. The nonlinearity of the exponential transform may yield nonuniformity in the reconstructed images. In order to minimize these errors, we will develop an alternative version of the inverse Cormack transform, instead of (11), to reconstruct the images.

It is also noted that the use of harmonic decomposition technique for SPECT imaging was investigated in [12] where the reconstruction was performed through the two-dimensional (2-D) Fourier transform (FT) of the sinogram. The possible application of the above angular harmonic technique for fan-beam geometry was mentioned in [13].

B. Alternative Version of the Inverse Cormack Transform Considering the Bandwidth

Here we will develop a new algorithm for the implementation of the inverse Cormack transform that is different from [12] and [13]. By this new algorithm, the computation of the derivatives of the projection data can be avoided, and the 2-D FT of the sinogram is reduced to a one–dimensional Fourier series expansion. In particular, the numerical computation of the new algorithm is efficient. Its performance is comparable to the filtered backprojection (FBP) algorithm [1]–[3].

The derivation of (9) needs skillful integral calculations, as shown in [9]. Here we notice that (9) can also be obtained by the use of the central slice theorem. The radon inversion formula can be rewritten as

$$\begin{aligned} f(r,\varphi) &= \int_0^{2\pi} d\theta \int_0^{\infty} p(l,\theta)\,dl \int_{-\infty}^{\infty} |\omega| e^{2\pi i\omega(r\cos(\theta-\varphi)-l)}\,d\omega \\ &= \int_0^{2\pi} d\theta \int_0^{\infty} \sum_{-\infty}^{\infty} p_n(l) e^{in\theta}\,dl \\ &\quad \times \int_{-\infty}^{\infty} |\omega| e^{2\pi i\omega(r\cos(\theta-\varphi)-l)}\,d\omega \\ &= \sum_{-\infty}^{\infty} e^{in\varphi} \int_0^{\infty} p_n(l)\,dl \int_{-\infty}^{\infty} |\omega|\,d\omega \\ &\quad \times \int_0^{2\pi} e^{in\theta+2\pi i\omega(r\cos\theta-l)}\,d\theta \\ &= \sum_{-\infty}^{\infty} e^{in(\varphi+\frac{\pi}{2})} \int_0^{\infty} p_n(l)\,dl \int_{-\infty}^{\infty} |\omega| e^{-2\pi i\omega l}\,d\omega \\ &\quad \times \int_0^{2\pi} e^{in\theta-2\pi i\omega r\sin\theta}\,d\theta \\ &= \sum_{-\infty}^{\infty} e^{in(\varphi+\frac{\pi}{2})} \int_0^{\infty} p_n(l)\,dl \int_{-\infty}^{\infty} |\omega| J_n(2\pi\omega r) e^{-2\pi i\omega l}\,d\omega \end{aligned} \tag{13}$$

where $J_n(\cdot)$ denotes the nth order Bessel function of the first kind. Expanding $f(r,\varphi) = \sum_{-\infty}^{\infty} f_n(r) e^{in\varphi}$, we have

$$f_n(r) = e^{in\frac{\pi}{2}} \int_0^{\infty} p_n(l)\,dl \int_{-\infty}^{\infty} |\omega| J_n(2\pi\omega r) e^{-2\pi i\omega l}\,d\omega. \tag{14}$$

By the uniqueness of the Fourier series expansion, (14) is equivalent to (9) or (11). In numerical implementation of (14), the main difficulty is calculating the term $\int_{-\infty}^{\infty} |\omega| J_n(2\pi\omega r) e^{-2\pi\omega l}\,d\omega$. However, in practical applications, the projection data $p(l,\theta)$ are usually sampled within a certain bandwidth. Thus, one only needs compute the integral $\int_{-\infty}^{\infty} |\omega| J_n(2\pi\omega r) e^{-2\pi\omega l}\,d\omega$ in the interval $[-C, C]$, where C is the bandwidth depending on the sampling interval. Then we have

$$\begin{aligned} &\int_{-\infty}^{\infty} |\omega| J_n(2\pi\omega r) e^{-2\pi i\omega l}\,d\omega \\ &\quad \approx \int_{-C}^{C} |\omega| J_n(2\pi\omega r) e^{-2\pi i\omega l}\,d\omega \\ &\quad = \int_0^{2\pi} e^{in\theta}\,d\theta \int_{-C}^{C} |\omega| e^{-2\pi i\omega(l+r\sin\theta)}\,d\omega. \end{aligned} \tag{15}$$

If the Shepp–Logan filter is used, then

$$\begin{aligned} &\int_{-\infty}^{\infty} |\omega| J_n(2\pi\omega r) e^{-2\pi i\omega l}\,d\omega \\ &\quad \approx \int_0^{2\pi} e^{in\theta} H_{\mathrm{SL}}(l+r\sin\theta, C)\,d\theta \end{aligned} \tag{16}$$

where

$$H_{\mathrm{SL}}(t,C) = \frac{C^2}{\pi^2}\left(\frac{1+\sin(C\pi t)}{1+2Ct} + \frac{1-\sin(C\pi t)}{1-2Ct}\right).$$

In an approximate form

$$f_n(r) \approx e^{in\frac{\pi}{2}} \int_0^{\infty} p_n(l)\,dl \int_0^{2\pi} e^{in\theta} H_{\mathrm{SL}}(l+r\sin\theta, C)\,d\theta \tag{17}$$

where $\int_0^{2\pi} e^{in\theta} H_{\mathrm{SL}}(l + r\sin\theta, C)\,d\theta = H_n(r,l)$ can be computed by an FFT. Equation (17) determines the same solution (in the numerical sense) as (11) for reconstructing $f(r,\varphi)$ using (6), but has several computational advantages as mentioned before.

C. A Translation Property of Fourier Series

To compute the Fourier coefficients $p_n(l)$ in (17) from the acquired data $P(\Phi, s)$, a translation property of Fourier series is needed. This property is described below. Suppose $g(x)$ is a 2π periodic function, then $g(x)$ can be expanded as

$$g(x) = \sum_{n=-\infty}^{\infty} g_n e^{inx}. \tag{18}$$

For every $\Delta \in (0, 2\pi)$, $g(x+\Delta)$ can also be expanded as

$$g(x+\Delta) = \sum_{n=-\infty}^{\infty} g_n^{\Delta} e^{inx}. \tag{19}$$

Then we have

$$g_n^{\Delta} = e^{in\Delta} g_n. \tag{20}$$

Equation (20) indicates that computing the Fourier coefficients of $g(x)$ is equivalent to computing the Fourier coefficients of $g(x+\Delta)$ through a translation.

D. Application to SPECT with Spatially Varying Focal Length Fan-Beam Collimators

All above arguments are based on a parallel-beam geometry. In this subsection, we will apply the previous procedure to the reconstruction for a spatially varying focal length fan-beam geometry. Reconstructing the image $f(r,\varphi)$ using (6) is equivalent to finding the Fourier coefficients $f_n(r)$, which are expressed by (17). The first step of the reconstruction is to compute the Fourier coefficients $p_n(l)$. The acquired projection data are expressed as $P(\Phi,\alpha)$ in the angular coordinate or $P(\Phi,s)$ in the distance coordinate, both of which are different from the desired form in (13), i.e.,

$$p_n(l)=\int_0^{2\pi} p(l,\theta)e^{-in\theta}\,d\theta. \tag{21}$$

The relation between l and s (or α) is illustrated in (4) [or (1)]. From the translation property of (20), the Fourier coefficients of $P(\Phi,s)$ (or $P(\Phi,\alpha)$) are equivalent to the Fourier coefficients of $p(l,\theta)$ through a translation factor $\frac{\pi}{2}+\tan^{-1}(\frac{s}{D(s)+R})$ (or $\frac{\pi}{2}+\alpha$). Therefore, the Fourier coefficients $p_n(l)$ can be derived by the translation of the Fourier coefficients of the acquired projection data $P(\Phi,s)$ or $P(\Phi,\alpha)$. The integral $\int\cdot dl$ in (17) can be numerically calculated by the trapezoidal rule. Thus, the Fourier coefficients $f_n(r)$ are completely determined through (17).

Summarizing the above arguments, we have the following computational procedures for the image reconstruction of spatially varying focal length fan-beam geometry by the alternative expression (17).

1) For fixed s_k, $\{P(\Phi,s_k)\}$ is sampled on $\{\Phi_j\}$, $j=0,1,2,\cdots,M-1$. Compute the FFT of $\{P(\Phi_j,s_k)\}$ with respect to the index j. After the translation $\frac{\pi}{2}+\tan^{-1}(\frac{s_k}{D(s_k)+R})$, we obtain the coefficients $p_n(l_k)$. Similar processing stage can be followed when using the angular coordinate (Φ,α).
2) Computing the inverse FFT of the filter $H_{\rm SL}(l+r\sin\theta, C)$ with respect to the variable θ for fixed r and l, we obtain $H_n(r,l)$. Notice that this step can be implemented before the data acquisition. The trapezoidal rule or Simpson's rule is used to compute the numerical integral $\int_0^\infty\cdot dl$ in (17). Thus $f_n(r)$ is obtained.
3) Given the coefficients $f_n(r)$, $f(r,\varphi)$ can be computed by the inverse FFT; see (6).
4) For visualization, interpolation is needed to interpolate $f(r,\varphi)$ into its Cartesian expression $f(x,y)$.

E. Comparison with the FBP Method of Parallel-Hole Collimator

For the parallel-beam geometry, the FBP method is expressed as [1]

$$f(r,\varphi)\approx\int_0^\pi d\theta\int_{-\infty}^{\infty}p(l,\theta)H_{\rm SL}\big(r\cos(\varphi-\theta)-l,C\big)\,dl. \tag{22}$$

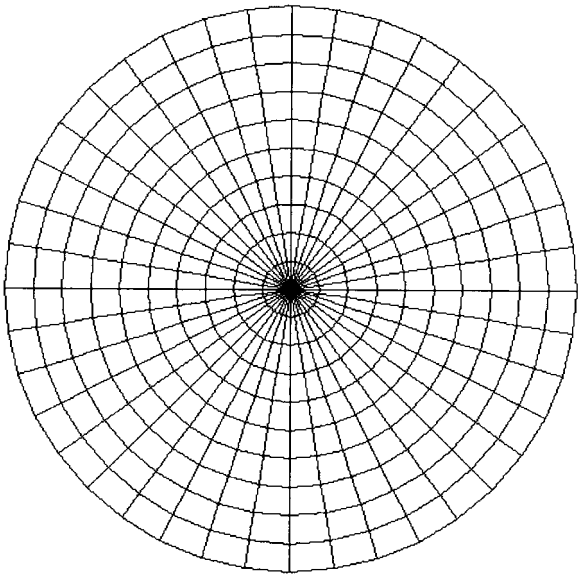

Fig. 4. The intersection points of the straight lines with the circles denote the sampled array (l_k,θ_j) in the projection space for the parallel-beam geometry. The position on each circle is specified by the angular variable θ. The radius of each circle is determined by the distance variable l. Both l and θ are uniformly sampled.

Because $p(-l,\theta)=p(l,\theta+\pi)$, (22) and (17) are equivalent, i.e.,

$$f_n(r)\approx e^{in\frac{\pi}{2}}\int_0^\infty p_n(l)H_n(r,l)\,dl. \tag{23}$$

Therefore, the presented algorithm (17) can be regarded as an implementation of the FBP method for spatially varying focal length fan-beam geometry by harmonic decomposition and has the similar numerical properties as the FBP algorithm. In other words, the reconstruction on the sampled array of Fig. 3 by the presented algorithm is similar to the reconstruction on the sampled array of Fig. 4 by the FBP method.

Figs. 3 and 4 indicate that the distribution of sampled points of a spatially varying focal length fan-beam geometry is less uniform than that of parallel-beam geometry. In the approximate sense, we could directly rebin Fig. 3 to Fig. 4 in the radon space. But this rebinning may generate interpolation errors and blur the reconstructed images. In this paper, this kind of interpolation is avoided by the use of the Fourier series translation. Therefore, it is expected that the developed algorithm should outperform the existing algorithms of rebinning Fig. 3 to Fig. 4 for the complicated data acquisition geometry of Fig. 1.

IV. Computer Simulations

Several computer simulations were performed to investigate the developed algorithm (17). In these simulations, a number of computer-generated projection data sets of a mathematically defined phantom was used. A display of the Shepp–Logan phantom by 128×128 digitization is shown in Fig. 5. All the reconstructed images will be displayed at the same digitization.

Projection Simulations: Simulations were performed for both a conventional fan-beam collimation and two different spatially varying focal length fan-beam geometries. In [5], the

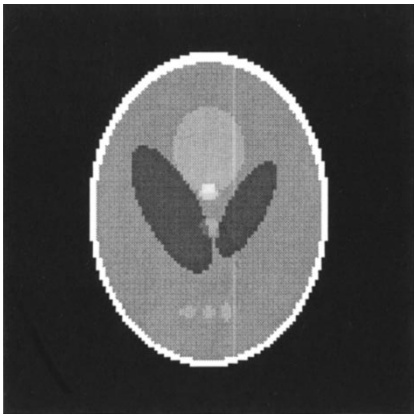

Fig. 5. The Shepp–Logan phantom by 128×128 digitization. This phantom is the sum of the gray values of ten ellipses. Each projection of this phantom can be analytically computed.

angular increments δ_1 and δ_2 were required to be the same. But according to the sampling theory of [14], such sampled points contain redundant information. Let C be the bandwidth in (15). To achieve the required resolution $\frac{2\pi}{C}$ [14] for a fan-beam geometry, the sampling intervals δ_1 and δ_2 in the angular coordinate should satisfy the following relations:

$$\delta_1 \le \frac{R_0 + D(0)}{R_0} \times \frac{\pi}{D(0)C} \quad \text{and} \quad \delta_2 \le \frac{\pi}{D(0)C}. \tag{24}$$

In the distance coordinate (Φ, s), $\delta_2 \le \frac{\pi}{C}$. The above sampling requirements were used to determine both δ_1 and δ_2.

In the simulations, Φ was sampled at 128 points evenly spaced in $[0, 2\pi]$, and the subtending angle $\alpha_0 \le \frac{\pi}{4}$. Both the angular expression (Φ, α) and the distance expression (Φ, s) were used to perform the computer simulations, where α and s were evenly sampled at 129 points over $[-\alpha_0, \alpha_0]$ and $[-s_0, s_0]$, respectively. The projection data were analytically computed from the Shepp-Logan phantom.

Reconstruction for a Conventional Fan-Beam Geometry: For a conventional fan-beam geometry, the distance function $D(s)$ should be a constant. Here we choose $D(s) = 3.0$ and $R = 2.0$, see Fig. 1. The object region is inside a disk with radius 2.0 centered at the origin. When the object region is digitized into a 128×128 pixel array, $R = 64$ pixel units, and the focal length $D(s) + R = 96$ pixel units. Choosing $s_0 = 5.0$, we have, from (4) and (5)

$$l = \frac{3.0s}{\sqrt{s^2 + 25.0}} \quad \text{and} \quad \theta = \Phi + \frac{\pi}{2} + \tan^{-1}\left(\frac{s}{5.0}\right). \tag{25}$$

The corresponding angular expressions are as follows, from (1)

$$l = 3.0 \sin\alpha \quad \text{and} \quad \theta = \Phi + \frac{\pi}{2} + \alpha \tag{26}$$

where $\alpha_0 = \pi/4$. This collimator/detector configuration is similar to that of the Trionix SPECT system.

The FBP method [2], [3] and the developed algorithm (17) were applied to reconstruct the images using projection data with equally spaced α and equally spaced s, respectively. The reconstructed images are shown in Fig. 6. The computation time was 7 s by the FBP method and 3 s by the proposed algorithm. These algorithms were coded by Visual C++ language in a Pentium II 266 PC computer. Here, the 3 s of the proposed algorithm include the computation of the coefficients $H_n(r, l)$. If these coefficients are precomputed, the reconstruction time can be less than 3 s.

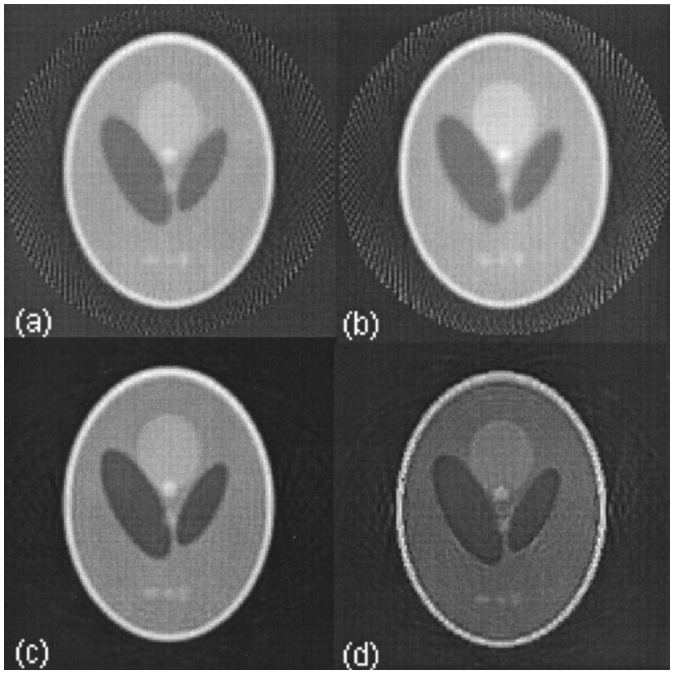

Fig. 6. The reconstructed images for a conventional fan-beam geometry: (a) and (b) by the FBP method, and (c) and (d) by the presented algorithm. The image densities were normalized to grey scales [0,256]. Since the images by the FBP method have large negative values, the zero background has risen by a noticeable gray level. The sampling of (a) and (c) is equiangular, while the sampling of (b) and (d) are equally spaced.

Notice that the different coordinate expressions yield slightly different results. The simulations indicate that the equiangular sampling yields better resolution than the equally spaced sampling by the FBP method. The reconstructed image in equally spaced sampling looks sharper than that with equiangular sampling by the proposed algorithm, but contains small edge artifacts. Fig. 6 indicates that the reconstructed images by the presented algorithm have a higher resolution than that by the FBP method for the same projection data. Also notice that different artifacts appear in the reconstructed images. The FBP method generates ray artifacts away from the center outside the object region, while the presented algorithm generates small ring artifacts outside the object region. In other simulations (not shown), we found that the bandwidth C should be chosen according to the sampling resolution, otherwise the ring artifacts would be serious. To compare the noise effect of the proposed algorithm with that of the FBP method, Poisson noise was added to the projection data. The total counts were approximately 8×10^7. The reconstructed images are shown in Fig. 7, where the results indicate that the proposed algorithm outperformed the FBP method.

Reconstruction for Spatially Varying Focal Length Fan-Beam Geometries: Two differently simulated spatially varying focal length fan-beam geometries were investigated. The focal length functions are as follows;

1) $D(s) = 2.5 + 0.8|s|$;
2) $D(\alpha) = 2.0/\cos\alpha$.

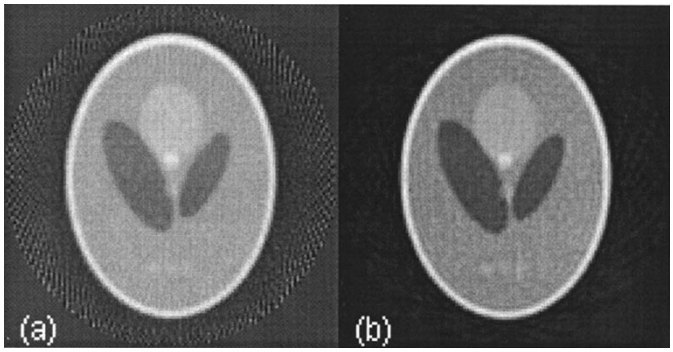

Fig. 7. The reconstructed images using equiangular sampling for the fan-beam geometry in the presence of Poisson noise of (a) the FBP method and of (b) the presented algorithm.

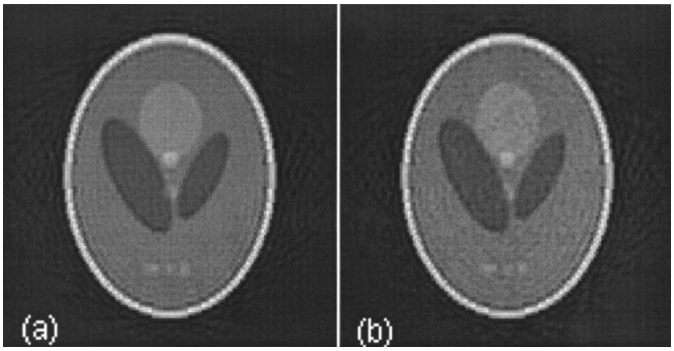

Fig. 8. The reconstructed images for the variable focal length function $D(s) = 2.5 + 0.8|s|$ using equally spaced collimation (a) without considering the Poisson noise and (b) in the appearance of the Poisson noise.

Function (I) was used in [8]. It increases slowly and linearly when $|s|$ uniformly increases. Function (II) increases fast and nonlinearly as $|\alpha|$ uniformly increases. As discussed previously, the spatially varying focal length fan-beam geometry should have this property: The focal lengths increase from a minimum at the center to a maximum at the edge of the object. Thus the spatially varying focal length collimator has good detection efficiency at the central region, and minimizes the truncation at the boundary area. Both functions 1) and 2) have this property with different speeds of variation. In the numerical simulations, the evenly sampled points of the variable s and α were used for focal length functions 1) and 2), respectively. To avoid the computation of the Jacobian of (2), numerical evaluation of $dl = l(s_k) - l(s_{k-1})$ or $dl = d(D(\alpha)\sin\alpha)$ was used to compute the numerical integral. The object region is still confined in a disk with radius 2.0 units centered at the origin. The proposed algorithm was tested for these two different acquisition geometries. The reconstructed images are shown in Figs. 8 and 9. The total counts were approximately 8×10^7. The simulations indicate that the proposed algorithm performs well for both acquisition geometries. The time for each reconstruction was 3 s on a Pentium 266 PC. As demonstrated in [6]–[8], the spatially varying focal length fan-beam geometry can improve the detection efficiency and reduce the artifacts due to the truncation of the projection data. The main reason of choosing spatially varying focal length fan-beam geometry is from physical considerations, and the goal of this paper is to look for an efficient reconstruction algorithm, such as (17).

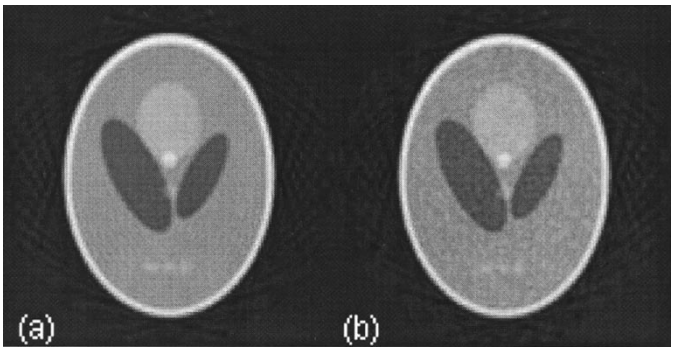

Fig. 9. The reconstructed images for the variable focal length function $D(\alpha) = 2.0/\cos\alpha$ under equiangular sampling (a) without considering the Poisson noise and (b) in the appearance of the Poisson noise.

V. Discussion and Conclusion

For parallel-beam projection data, the integrals in the right side of (22) can be calculated sequentially. But if the acquisition geometry becomes complicated as shown in Fig. 1, it has been proven [5] that we can not compute (22) sequentially, so a double integration is necessary [7]. This indicates that much more computation time is required. For example, if r, φ, l, and θ are all sampled as N points, then the total number of products in (22) is C_1N^4 (hereafter, C_i is a fixed constant depending only on a specific algorithm). In this paper, a harmonic decomposition algorithm was developed to reduce the computational burden. Since the FFT can be used to compute the Fourier coefficients $p_n(l)$, the total number of products is reduced to $C_2N^3\log_2 N$. If the coefficients $H_n(r,l)$ are computed before the data acquisition, the number of products would be C_2N^3, the same level as that of the FBP method. Therefore, the presented harmonic decomposition algorithm for spatially varying focal length fan-beam geometry can have a similar computational efficiency as the FBP method for parallel-hole collimators. In particular, it was found that the computational time by the developed algorithm is less than that by the FBP method for the conventional fan-beam geometry when using 128×128 image arrays. It is also noted that there exist differences between the reconstructions with equiangular data sampling and with the equally spaced data sampling. The presented simulations indicated that the former sampling yields smoother images, while the later one generates sharper images but containing small edge artifacts. In addition to the complicated geometry, the proposed algorithm is also new for both the conventional parallel- and fan-beam geometries.

Acknowledgment

The authors would like to thank Dr. G. Gindi and Dr. C. Roque for refining the English and making this paper more readable. The authors also express their deep appreciation to the anonymous reviewers for their helpful criticisms and constructive suggestions.

REFERENCES

[1] L. A. Shepp and B. F. Logan, "The Fourier reconstruction of a head section," *IEEE Trans Nucl. Sci.*, vol. 21, pp. 21–43, 1974.

[2] G. T. Herman and A. Naparstek, "Fast image reconstruction based on a radon inversion formula appropriate for rapidly collected data," *SIAM J. Appl. Math.*, vol. 33, pp. 511–533, 1977.

[3] B. K. Horn, "Fan-beam reconstruction methods," in *Proc. IEEE*, 1979, vol. 67, pp. 1616–1623.

[4] G. T. Gullberg, C. R. Crawford, and B. M. W. Tsui, "Reconstruction algorithm for fan-beam with a displaced center-of rotation," *IEEE Trans. Med. Imag.*, vol. 5, pp. 23–29, 1986.

[5] J. You, S. Bao, and Z. Liang, "Benefits of angular expression to reconstruction algorithms for collimators with spatially varying focal lengths," *IEEE Trans. Med. Imag.*, vol. 16, pp. 527–531, 1997.

[6] G. L. Zeng, G. T. Gullberg, R. J. Jaszczak, and J. Li, "Fan-beam reconstruction algorithm for a spatially varying focal length collimator," *IEEE Trans. Med. Imag.*, vol. 12, pp. 575–582, 1993.

[7] Z. Cao and B. M. W. Tsui, "An analytical reconstruction algorithm for multifocal converging-beam SPECT," *Phys. Med. Biol.*, vol. 39, pp. 281–291, 1994.

[8] G. L. Zeng and G. T. Gullberg, "A backprojection filtering algorithm for a spatially varying focal length collimator," *IEEE Trans. Med. Imag.*, vol. 13, pp. 549–556, 1994.

[9] A. M. Cormack, "Representation of a function by its line integrals, with some radiological applications," *J. Appl. Phys.*, vol. 34, pp. 2722–2727, 1963.

[10] ———, "Representation of a function by its line integrals, with some radiological applications II," *J. Appl. Phys.*, vol. 35, pp. 195–207, 1964.

[11] E. W. Hansen, "Theory of circular harmonic image reconstruction," *J. Opt. Soc. Am.*, vol. 71, pp. 304–308, 1981.

[12] W. G. Hawkins, P. K. Leichner, and N. C. Yang, "The circular harmonic transform for SPECT reconstruction and boundary conditions on the Fourier transform of sinogram," *IEEE Trans. Med. Imag.*, vol. 7, pp. 135–148, 1988.

[13] R. M. Lewitt, "Reconstruction algorithms: Transform methods," in *Proceeding of the IEEE*, 1983, vol. 71, pp. 390–408.

[14] F. Natterer, "Sampling in fan-beam tomography," *SIAM J. Appl. Math.*, vol. 53, pp. 358–380, 1993.